

# Evolution of the Climate Forcing During the Two Years after the Hunga Tonga-Hunga Ha'apai Eruption

M. R. Schoeberl<sup>1†</sup>, Y. Wang<sup>1</sup>, G. Taha<sup>2</sup>, D. J. Zawada<sup>3</sup>

R. Ueyama<sup>4</sup> & A. Dessler<sup>5</sup>

<sup>1</sup>Science and Technology Corporation, Columbia, MD, USA

<sup>2</sup>Morgan State University, Baltimore, MD, USA

<sup>3</sup>Institute of Space and Atmospheric Studies, University of Saskatchewan, Saskatoon, SK, Canada

<sup>4</sup>NASA Ames Research Center, Moffett Field, CA, USA

<sup>5</sup>Texas A&M University, College Station, TX, USA

Corresponding Author: M. R. Schoeberl (mark.schoeberl@mac.com)

<sup>†</sup>Science and Technology Corporation, 10015 Old Columbia Road, Suite E-250, Columbia, MD, 21046, USA

## Key Points

- The Jan. 15, 2022, Hunga eruption increased aerosols and H<sub>2</sub>O in the southern hemisphere stratosphere and then dispersed throughout 2022/3.
- Stratospheric water vapor, ozone, temperature, and aerosol optical depth contribute to the change in downward radiative fluxes.
- Hunga produced a global change in tropopause downward radiative flux of -0.17 and  $\pm 0.07$  W/m<sup>2</sup> over the two-year period.

## Abstract

We calculate the climate forcing for the two years after the January 15, 2022, Hunga Tonga-Hunga Ha’apai (Hunga) eruption. We use satellite observations of stratospheric aerosols, trace gases and temperatures to compute the tropopause radiative flux changes relative to climatology. Overall, the net downward radiative flux decreased compared to climatology. Although the Hunga stratospheric water vapor anomaly increases the downward infrared radiative flux, the solar flux reduction due to Hunga aerosol shroud dominates the net flux over most of the two-year period. Decreases in temperature produced by the Hunga stratospheric circulation changes contributes to the decrease in downward flux; however, the Hunga induced decrease in ozone increases the net short-wave downward flux creating small sub-tropical net flux increase in late 2022. Coincident with the aerosols settling out, the water vapor anomaly disperses, and circulation changes disappear so that the contrasting forcings all decrease together. By the end of 2023, most of the Hunga induced radiative forcing changes have disappeared. There is some disagreement in the satellite stratospheric aerosol optical depth (SAOD) which we view as a measure of the uncertainty; however, SAOD uncertainty does not alter our conclusion that, overall, aerosols dominate the radiative flux changes followed by temperature and ozone.

## Plain Language Summary

The Hunga Tonga-Hunga Ha’apai (Hunga) submarine volcanic eruption on January 15, 2022, produced aerosol and water vapor plumes in the stratosphere. These plumes have persisted mostly in the Southern Hemisphere throughout 2022 and into 2023. Enhanced tropospheric warming due to the added stratospheric water vapor is offset by the larger stratospheric aerosol attenuation of solar radiation. Hunga induced circulation changes that reduce ozone stratospheric ozone and lower temperatures also play a role in the net forcing. The change in the radiative flux could result in a very slight 2022/3 cooling in Southern Hemisphere. The Hunga climate forcing has decreased to near zero by the end of 2023.

## Index Terms

0340 Middle atmosphere dynamics

0341 Middle atmosphere: constituent transport and chemistry

0370 Volcanic effects

## 1. Introduction

The eruption of the Hunga Tonga-Hunga Ha’apai (Hunga) (20.54°S, 175.38°W) submarine volcano on Jan. 15, 2022, sent material to the mesosphere (Proud et al., 2022; Carr et al., 2022). Microwave Limb Sounder (MLS) measurements (Millán et al., 2022,

hereafter M22; Santee et al., 2023) and balloon sondes measurements (Vomel et al. 2022) showed that a significant amount of water vapor was injected by the eruption into the tropical Southern Hemisphere (SH) mid-stratosphere. Hunga also injected at least 0.5 Tg of SO<sub>2</sub> into the stratosphere (Carn et al., 2022) although this amount may have been as much as 1.5 Tg (Sellitto et al., 2024). The SO<sub>2</sub> oxidation forms a sulfate aerosol layer that was detected by the Ozone Mapping and Profile Suite limb profiler (OMPS) (Taha et al., 2022) shortly after the eruption. The MLS estimated Hunga water injection was unprecedented, up to 146 Tg or ~10% increase in the total stratospheric water vapor prior to the eruption (M22). The water vapor and aerosol plumes from the HT eruption have persisted in the SH throughout 2022 (Schoeberl et al., 2023a, b, hereafter S23a,b). The presence of water vapor led to a stratospheric cooling of ~ 4 K in March and April (Schoeberl et al., 2022, hereafter S22) due to the increased outgoing IR radiation. This cooling produces a secondary circulation (Coy et al., 2023) that produced temperature and ozone anomaly (Wang et al., 2023) in mid 2022.

The volcanically generated abundance of stratospheric aerosols causes a reduction in solar radiative forcing and, if large enough, a decrease in tropospheric temperatures (Aurby et al., 2021; Stenchikov, 2016; Hansen et al., 2002) which has been observed (Fujiwara et al., 2020, Crutzen, 2006, Robock, 2000). Volcanic aerosols can persist in the stratosphere for years and even self-loft through solar heating when the aerosols are mixed with ash (Khaykin et al., 2022).

Changes in stratospheric water vapor can also cause changes in climate forcing (Forster and Shine, 1999). Solomon et al. (2010) showed that the 10-year lower tropical stratospheric decrease of ~0.4 ppmv H<sub>2</sub>O in the tropical between 2000 and ~2005 would reduce tropospheric forcing by ~0.098 W/m<sup>2</sup> or about ~ 0.245 W/m<sup>2</sup>/ppmv. The water vapor radiative forcing results from changes in the thermal IR emission and solar flux absorption. The solar flux absorption by water vapor is generally smaller than the thermal emission. Extending the Solomon et al. (2010) study, Dessler et al. (2013) determined calculated a water vapor climate feedback parameter of 0.27 W/m<sup>2</sup>/ppmv. Banerjee et al. (2019) analyzing CMIP5 models computed the stratospheric water vapor component of the climate feedback parameter to be 0.14 W/m<sup>2</sup>/K for 4xCO<sub>2</sub>. Li and Newman (2020) using the Goddard Earth Observing System Chemistry-Climate model computed a similar 4xCO<sub>2</sub> stratospheric water vapor feedback value of 0.11 W/m<sup>2</sup>/K.

Given the sensitivity of the climate to stratospheric water vapor, it is logical to assume that Hunga might have a significant climate impact. Jenkins et al. (2022) used a parameterized climate-response model to investigate the climate impact of the Hunga water vapor plume. They neglected the impact of aerosols and only considered the radiative forcing due to the water vapor injection and computed a 0.12 W/m<sup>2</sup> increase in tropospheric radiative forcing. However, Sellitto et al. (2022) and Zhu et al. (2023) roughly estimated that the aerosol plume would produce a peak solar forcing reduction of ~1.7-1.8 W/m<sup>2</sup>, exceeding the estimated of H<sub>2</sub>O forcing. S23b provided a more accurate estimate confirming that the aerosols overwhelmed the water vapor flux increase during the first year following the eruption.

In this study we extend the S23b computation of the radiative forcing into the second year following the Hunga eruption. Our basic approach is the same as S23b, but in addition we break out the various radiative forcing components in more detail. As before we use the OMPS measurements of stratospheric aerosol extinction (Taha et al., 2022) to compute the stratospheric aerosol optical depth (SAOD), but we also compare NASA OMPS SAOD to the Stratospheric Aerosol and Gas Experiment III on the international space station (SAGE III/ISS) measurements of SAOD, and OMPS data processed by U. of Saskatchewan (USask) algorithm. The USask OMPS data are processed using a tomographic retrieval scheme (Bourassa et al., 2023) that is different from the NASA algorithm. The tomographic retrieval has the advantage of correcting OMPS measurements for distortion around the edges of aerosol and cloud anomalies (see Gorkavyi et al., 2021). We refer to these data as USask OMPS.

To estimate the trace gas radiative forcing we use the AER rapid radiative transfer model (RRTM, Mlawer et al., 1997) to compute the changes in shortwave and longwave fluxes at the tropopause. Our approach is to use the prior 10-year climatology (2012-2021) of MLS trace gases and temperatures and then swap in the changes observed by MLS in the 2022-2023 period to compute the relative change in radiative forcing for each component. This allows us to quantify the relative importance of various processes contributing to the overall radiative impact. We focus on the downward longwave and shortwave flux changes at the tropopause relative to a 10-year climatology. In general, longwave IR radiation from the mid-stratosphere will be absorbed in the cold upper troposphere whereas shortwave radiation will penetrate to the surface. The tropospheric climatic response to these flux changes is beyond the scope of this study. Our goal is to determine the net flux changes at the tropopause as the Hunga plume evolves.

## 2. Observational Data Sets

We use Microwave Limb Sounder (MLS) V5 for temperature and trace gas observations. The data quality for the Hunga anomaly is detailed in M22 and MLS data is described in Livesey et al. (2021). Other trace gases changes are described in Santee et al. (2023). We restrict our constituent analysis to below 35 km well above the maximum Hunga water vapor anomaly (~25 km). In addition, the climate forcing due water vapor emissions above 30 km is negligible (Solomon et al., 2010). The daily MLS data sets are averaged onto a 5°x10° latitude-longitude grid.

We use NASA OMPS level-2 V2.1 aerosol extinction data (Taha et al., 2021) which provides aerosol retrievals up to 40 km. Although the extinction measurements by OMPS V2.1 are generally consistent with those made by SAGE III/ISS (Taha et al., 2021), as shown in Gorkavyi et al. (2021), the NASA OMPS algorithm may overestimate the aerosol extinction at the edges and below eruption clouds because of the limb viewing geometry. Bourassa et al. (2023) developed a tomographic retrieval scheme that corrects for the OMPS viewing geometry problems, and the USask OMPS retrieved Hunga extinction levels are roughly a factor of two smaller than NASA OMPS for the first four months after the eruption. As Bourassa et al (2023) noted the aerosol distribution is

becomes more zonal after the first four months, the aerosol edges are disappearing and the differences between the two extinction estimates is becomes smaller.

For both NASA OMPS and USask OMPS, we integrate the 745 nm extinction from the 1 km above the tropopause to 35 km to obtain SAOD. We use extinction measurements at 745 nm since this wavelength has good sensitivity to small particles and is less contaminated by Rayleigh scattering than shorter wavelengths (Taha et al., 2021). The tropopause information comes from the Modern-Era Retrospective analysis for Research and Applications, Version 2 (MERRA2, see Gelaro et al., 2017). We start the integration above the tropopause to eliminate the extinction by thin clouds near the tropopause. Daily data are interpolated onto a 2° latitude zonal mean daily grid; we use a 10 day box-car smoother to reduce measurement noise.

We use the S23b algorithm to convert SAOD to solar flux reduction; the algorithm uses the 550nm SAOD. To convert the SAOD at the 745 nm wavelength to 550nm we use the Ångström exponent from SAGE III/ISS (Cisewski et al., 2014) calculated using extinction coefficients at 550 nm and 756 nm. We use the SAGE Ångström exponent instead of one derived from OMPS, because the OMPS Ångström exponent appears inconsistent with the SAGE Ångström exponent likely due to limitation of the shorter wavelength retrievals in the SH and lower altitudes, and, to some extent, the algorithm's particle size assumptions.

### **3. Analysis of Hunga Climate Impact**

#### **3.1 Changes in constituent distributions and temperatures following Hunga eruption.**

To interpret the changes in downward radiative fluxes, we need to assess how the constituent distribution and temperatures change following the eruption relative to climatology. Some of these changes are part of year-to-year variability in the stratosphere (e.g. the quasi-biennial oscillation, QBO), whereas others are induced by the Hunga water vapor and aerosol anomalies. Figure 1 shows the equatorial time series of aerosols, water vapor, ozone, and temperature. Overlaid on each figure is the equatorial zero wind line, showing the descent of the westerly phase of the QBO starting in April 2022, and the easterly phase starting in April 2023.

Fig. 1a shows that aerosols enter the tropical region shortly after the Hunga eruption on Jan. 15, 2022. The aerosol concentration gradient follows the zero-wind line downward as the meridional circulation associated with the QBO pushes aerosols southward (Schoeberl et al., 2023a). In contrast, Figure 1b shows that the water vapor anomaly moves steadily upward as part of the Brewer-Dobson (BD) circulation. The usual tape-recorder signal is also evident in the figure with ascending smaller water vapor anomalies in August 2022, May 2023, and August 2023.

Associated with the QBO westerly descent Fig. 1c shows an ozone increase moving with the zero-wind line. This ozone increase is also associated with the QBO secondary

circulation (Plumb and Bell, 1982) which advects higher concentration of ozone downward and creates a warm temperature anomaly seen in Fig. 1d. The reverse occurs for the descending QBO easterly phase in 2023.

Figure 2 shows the time series as in Fig. 1 but at 40°S. Aerosols and water vapor arrive at this latitude mostly after May 2022. This latitude is too far from the equatorial QBO to be influenced by its secondary circulation. However, the water vapor anomaly is strongly correlated with a decrease in ozone and temperature starting in May 2022 and ending in December 2022. Wang et al. (2023) shows that this anomaly is the result of a weakening of the descending branch of the BD circulation due to *in situ* radiative cooling associated with Hunga water vapor. The descending branch transports ozone from higher altitudes into the middle stratosphere and adiabatically warms the region. As the BD circulation weakens, both an ozone and temperature anomaly form. Later, the water vapor anomaly disperses, and as the summer SH BD circulation weakens, the anomaly fades.

Figure 3 shows OMPS 745 nm aerosol extinction coefficient at 20 km, as well as water vapor at 25 km along with changes in ozone and temperature relative to the 10-year MLS climatology at 25 km. This figure provides a third perspective on constituent changes. The aerosol and water vapor anomalies stay isolated in the SH except for some initial transport into the Northern Hemisphere (NH) shortly after the eruption (S23a). The tropical temperature decrease in Feb.-April 2022 is due to radiative cooling by water vapor (Schoeberl et al., 2022). The changes in ozone at the equator – the increase in May-September 2022 and decrease in the same months in 2023 are associated with the QBO circulation moving downward through this altitude region.

In the SH extra-tropics, the March 2022 temperature (Fig. 3c) decrease is due to water vapor cooling (S22), but the later temperature and ozone decrease further south is the result of the weakening BD circulation mentioned above (Wang et al., 2023). Under normal conditions, BD circulation adiabatically heats the extra-tropics and advects ozone into the lower stratosphere. The weaker BD circulation thus causes a temperature and ozone decrease.

## 3.2 Aerosol Direct Forcing

### 3.2.1 Aerosol measurements.

The S23b parameterization scheme is used to compute the direct solar forcing. This scheme, as do the schemes shown in Table 1, uses the SAOD at 550 nm derived from extinction measurements at 745 nm and converted to 550 nm using the SAGE Ångström exponent. Figure 4 shows time series of the NASA OMPS 745 nm SAOD (4a), the USask 745 nm SAOD (4b), and SAGE III/ISS 756 nm SAOD (4c). The SAGE measurements are interpolated to the OMPS regular grid, but we show the SAGE measurement points to show where the interpolation is filling in missing data. Figure 4d compares the OMPS SAOD measurements converted to 550nm at 20°S and the SAGE 550 nm SAOD measurements interpolated to the OMPS grid.

Figure 4 shows the range of SAOD values with USask nearly a factor of two smaller than NASA OMPS after the eruption. above, the main difference between the two OMPS SAOD values is that USask corrects for the effects of inhomogeneity along the line of sight (Bourassa et al., 2023), although differences can also be caused by the difference between size distribution assumptions built into the two algorithms. However, from the SAGE measurements, it is apparent that USask is low biased while the NASA is high biased. Figure 4d shows that after August 2022, NASA OMPS comes into agreement with SAGE and all three SAOD estimates converge in mid-2023. (The slower rise in SAGE SAOD after the eruption; this is due to the SAGE measurement pattern which missed the initial eruption latitude.) We view the differing SAOD estimates as a measure of the uncertainty. In our forcing estimates below, we will show results with both NASA OMPS SAOD and USask SAOD – these tend to bracket the SAGE estimates.

The evolution of the SAOD reflects the evolution of the aerosol distribution shown in Fig. 3a (also Taha et al., 2022). Both SAOD distributions show an initial high value between 30°S and the equator until May-June when the SAOD shifts south. This shift is also apparent aerosols at 20 km (Fig. 3a). The southward shift is due to increased seasonal eddy transport. In April-July 2023, NASA OMPS shows a new anomaly in SAOD. This anomaly is less evident in the USask product but is still present. The source of this anomaly is unknown but may be a movement of Hunga aerosols toward mid-latitudes with the formation of the Antarctic polar vortex. No SH volcanic eruptions occurred during this period. In any event, the exact source of this anomaly is uncertain. By the end of 2023 the SAOD anomalies have largely disappeared.

### 3.2.2 Direct forcing parameterization

A variety of parameterizations have been used to convert global averaged SAOD into global average solar direct forcing change ( $\Delta A$ ) as shown in Table 1. These parameterizations take the form  $\Delta A = -R \text{ SAOD (550nm)}$ .

Table 1 Parameterization for SAOD Solar Forcing	
Reference	R
Hansen et al. (2002)	21
Yu and Huang (2023)	29.5 – Clear 15.7 – All sky
Yu et al. (2023)	23
S23b linear-log fit	19.5 SAOD < 0.015
	5.58+1.26 log <sub>e</sub> (SAOD) SAOD > 0.015

The linear parameterizations tend to underestimate the forcing of mid-sized eruptions (e.g. El Chichón, SAOD of ~0.05;) and overestimate very large eruptions (e.g. Pinatubo, SAOD of 0.2, Pitarai et al., 2006). The Yu and Huang (2023) parameterization was

developed from MERRA2 tropospheric AOD estimates during a non-volcanic period. In their nomenclature, ‘Clear’ assumes no cloud reflectivity whereas ‘All sky’ includes climatological cloud distributions. Most estimates of direct solar forcing changes do not include cloud effects because the solar flux impact of clouds is considered a separate uncertainty (Hansen et al., 2002). In this study, we will use the Yu and Huang (2023) algorithm to estimate the impact of clouds on the Hunga direct forcing as was done in S23b. We multiply  $\Delta A$  by the cosine of minimum solar zenith angle as a function of day to approximate the change in solar forcing. Shortwave forcing computed by the RRTM includes the zenith angle variations.

Figure 5 shows the estimated reduction in solar forcing using NASA OMPS and USask OMPS. The southward movement of the aerosol distribution in May 2022 is reflected in the forcing shift. We also see a slight increase in forcing due to the April-July 2023 aerosol anomaly.

### 3.3 Flux changes due to trace gases and temperatures

In S23b we only considered the water vapor shortwave and longwave IR downward flux changes at the tropopause relative to a 5-year MLS water vapor climatology. Here we include the changes due to temperature, ozone, and water vapor relative to a 10-year MLS climatology. The climatology averages out the QBO induced changes in temperature as well as any year-to-year stratospheric variability that would normally occur. This means that some of our computed radiative flux anomalies may be due to processes not associated with Hunga trace gas anomalies (e.g. the QBO).

Our approach is to take the 10-year climatology of temperature and trace gases, then insert the one of the 2022/3 anomalies fields and compare the changes in tropopause downward fluxes to the climatology. For example, we insert the observed 2022/3 water vapor anomaly into the climatology and compare the altered downward fluxes to the downward flux climatology. This works well for isolating the effects of the Hunga water vapor since seasonal variations in stratospheric water vapor is normally  $\sim 10\%$  and Hunga anomalies were up to 5 times large than the climatology. For ozone and temperature this approach is more problematic since large natural changes occur that may be unrelated to Hunga (e.g. the tropical QBO (Baldwin et al., 2001) and extra-tropical stratospheric warmings (Veenus et al., 2023; Tao et al., 2015)).

#### 3.3.1 Water vapor

The Hunga stratospheric water vapor anomaly will increase the tropopause downward long-wave IR flux and reduce the short-wave flux (Solomon et al., 2010). Figure 3a shows the zonal mean water vapor anomaly at 25 km, and Fig. 6 shows the corresponding changes in downward flux at the tropopause. The longwave increase is shown in Fig. 6a and the shortwave decrease is shown in Fig. 6b. The change in  $H_2O$  shortwave flux combines with the aerosols to reduce the direct solar forcing. The increased longwave flux, on the other hand, is absorbed in the upper troposphere where the temperatures are significantly colder than the emitting region. Figure 6b shows that the increased long



334 wave flux is on the order of  $\sim 0.6 \text{ W/m}^2$  which is smaller than the aerosol reduction of  
335 direct solar forcing (Fig. 5).

### 336 3.3.2 Ozone

337 Figure 3b shows the changes in ozone at 25 km and Fig. 7 shows the changes in the  
338 downward flux. The changes in ozone are mostly driven by changes in circulation either  
339 natural or by the secondary circulation produced by the *in situ* radiative cooling  
340 associated with the water vapor anomaly (Santee et al., 2023; Wang et al., 2023). Smaller  
341 ozone change may also be due to altered chemical processes (Wilmouth et al., 2023).  
342

343 As discussed in Section 3.1, ozone changes at the equator (Figs. 1c, 3b) are due to the  
344 descending westerly and then easterly QBO phases. In the SH extra-tropics, a decrease in  
345 ozone occurs from March 2022 through October 2022 due to the relative weakening of  
346 the downward branch of the downward BD circulation by water vapor radiative cooling  
347 (Coy et al., 2022; Wang et al., 2023).  
348

349 Fig. 7 shows that increases in ozone cause a decrease in shortwave tropopause flux and  
350 an increase in longwave tropopause flux. The reverse is true for decreases in ozone. As  
351 expected, Figure 7a shows a small increase in downward longwave IR flux associated  
352 with the QBO driven ozone enhancement. A larger broader decrease in IR flux is  
353 associated with the southern extra-tropical ozone decrease. The longwave flux changes  
354 are small relative to the changes due to water vapor (Fig. 6b). In contrast, Fig. 7b shows  
355 the shortwave flux changes are larger than the water vapor shortwave flux changes. The  
356 equatorial short-wave ozone flux changes are also mostly associated with the QBO with a  
357 relatively large flux decrease at the equator and a smaller flux increase in the southern  
358 extratropical latitudes associated with the decrease of ozone. The shortwave ozone flux  
359 changes are on the scale of the aerosol flux changes (Fig. 5).  
360

### 361 3.3.3 Flux Changes due to Temperature

362 The changes in stratospheric temperature also alter the downward longwave fluxes by  
363 radiatively important trace gases even though the gas concentrations are not significantly  
364 altered by the eruption (e.g.  $\text{N}_2\text{O}$  see Santee et al. (2023), Fig. 1). To estimate the  
365 tropopause downward flux changes due to temperature changes, we use the  
366 climatological trace gas concentration and swap in the 2022/3 temperatures. Figs. 3a  
367 shows the 25 km temperature differences from climatology.  
368

369 Fig. 8 shows the temperature induced change in downward longwave fluxes. The  
370 shortwave flux is not directly affected by the temperature changes and is not shown. The  
371 flux change mirrors the temperature anomalies shown in Fig. 3a especially the impact of  
372 the extra-tropical SH cooling from March 2022 - November 2022. As mentioned in  
373 Section 3.1, this temperature anomaly is due to the weaker BD circulation and produces a  
374 significant decrease in downward long-wave flux. In general, the changes in stratospheric  
375 temperature are as large or larger than the downward long-wave flux than trace gas  
376 anomalies.  
377  
378  
379

### 3.4 Combined Fluxes

#### 3.4.1 Total flux changes

Figure 9 shows the total estimated tropopause flux changes following the Hunga eruptions. We combine the temperature and trace gas shortwave and longwave downward fluxes with the aerosol direct forcing changes. As with the aerosol direct forcing, short wave forcing by ozone and water vapor is weighted by the solar zenith angle.

Figure 9a shows the zonal mean flux vs time using the NASA OMPS SAOD, while Fig. 9b shows the zonal mean fluxes using the USask OMPS SAOD, and parts 9c-e show the component fluxes at the equator, 20°S and 40°S associated with Fig. 9a. The component picture shows aerosols dominating the forcing with changes in temperature and ozone (short wave) contributing next. The long-wave water vapor heating, the focus of Jenkins et al. (2022), appears to be one of the least important components of the total flux after the first few months.

Figure 9 shows that there is net SH cooling through most of the two-year period with either NASA or USask SAOD. The exception is near 20° S in Fig. 9b,d where the fluxes are slightly positive from August – November 2022. This is the period where the aerosol distribution shifts southward and the increase in ozone short-wave flux exceeds the aerosol decrease. Aerosols and short-wave flux variations in ozone and long wave flux variations in temperature dominate the total flux changes. Recall that these flux changes are relative to the 10-year climatology. Thus, some of these changes are natural (e.g. QBO) and some generated by the Hunga anomalous circulation (Wang et. al., 2023).

Fig. 4a shows that the Hunga SAOD anomaly persists into the beginning of 2023 then reaches a small second peak at higher latitudes in May 2023. This second peak shows up in the forcing (Fig. 9a,e). The combination of aerosol direct forcing, temperature changes and ozone recovery lead to net decrease in downward flux in 2023. By the end of 2023 the aerosol forcing has dwindled to near zero. Fluctuations in the 2023 forcing components, aside from aerosols, appear to be mostly due to year-to-year variability.

#### 3.4.2 All Sky Albedo

Yu and Huang (2023) developed a cloud correction for SAOD direct forcing (all sky albedo) which essentially includes cloud reflection of solar radiation before it can reach the surface. Most papers computing aerosol impact of volcanic emissions or fires do not include cloud effects in computing the direct forcing. In our computation, cloud reflectivity is applied to all the short-wave fluxes, thus all sky albedo reduces the shortwave ozone and water vapor forcing as well as the aerosol direct effect. Fig. 10a shows the impact of all sky albedo on the total forcing using NASA SAOD, and Fig 10b shows the results using USask SAOD. These figures should be compared to Fig. 9a,b, respectively. The USask SAOD case shows the smallest net forcing as expected.

#### 3.4.3 Global and Hemispheric Forcing

To estimate the global forcing, we integrate the downward flux from  $\pm 60^\circ$ . The hemispheric flux is computed from  $60^\circ$  S to the equator and from the equator to  $60^\circ$  N. In Fig. 11 we show the two extreme cases – NASA OMPS SAOD clear skies and USask OMPS with all sky albedo to provide an estimate of the uncertainty in the forcing. The two cases are shown in Fig. 9a and Fig. 10b. The 2022/2023 peak and average radiative forcing is summarized in Table 2.

Our results show that most of the period there is global net cooling, except for the Jan-Feb. 2022 period right after the eruption, when the water vapor forcing peaked, and before most of the aerosol shroud has formed. A second region of very slightly positive forcing occurs  $10^\circ$ - $40^\circ$ S June-December 2022 where decreases in ozone generate an increase in tropopause shortwave flux.

The Jan-Feb. 2022 global flux increases occurs when a NH warming– not connected with Hunga (Fig. 3a) - exceeds the SH cooling. We also note that from Figs. 9,10 and Table 2, the aerosol reduction in direct forcing is largest in the SH where to which the aerosols are confined through most of the post eruption period (Fig. 5). We conclude that the Hunga peak global forcing is  $-0.475 \pm 0.145$  W/m<sup>2</sup>. In contrast, the Pinatubo global forcing was  $\sim -3.5$  W/m<sup>2</sup> (Pitari et al., 2016), about 6-12 times larger than Hunga.

Table 2. Forcing amounts in W/m<sup>2</sup>

Forcing	Peak Global	Peak SH	Peak NH	Average Global	Average SH	Average NH
NASA OMPS Clear Sky	-0.59	-0.75	-0.47	-0.24	-0.43	-0.05
USask OMPS All Sky	-0.3	-0.55	-0.39	-0.1	-0.21	0.01
Average	$-0.47 \pm 0.14$	$-0.65 \pm 0.10$	$-0.43 \pm 0.04$	$-0.17 \pm 0.07$	$-0.32 \pm 0.11$	$-0.025 \pm 0.02$

## 4.0 Summary and Conclusions

We have extended the S23b estimate of the Hunga radiative forcing through 2023. We have also added the changes in the long-wave and short-wave ozone and long-wave temperature radiative fluxes to our estimates. We note that there are differences between the SAOD estimates from NASA OMPS retrievals (Taha et al., 2021) and USask tomographic retrievals (Bourassa et al., 2023) post-Hunga. Both retrievals show contrasting bias compared to SAGE III/ISS SAOD measurements (Fig. 4d) in the first half of 2022, before the aerosol distribution has become zonal. After mid 2022 the NASA and USask algorithms are in better agreement. We account for the SAOD

differences by performing radiative forcing estimates for both NASA and USask SAOD retrievals as a measure of the forcing uncertainty. We also account for tropospheric cloud albedo using the Yu and Huang (2023) parameterization as was done in S23b.

Our earlier conclusion (S23b) that the 2022/2023 global Hunga impact is a reduction in tropopause flux remains valid even with the aerosol uncertainty and ozone/temperature effects included. As we previously found, the tropopause flux reduction is largely due to the aerosol shroud which is mostly confined to the SH. Lower stratospheric SH Hunga induced temperature changes (Wang et al., 2023; Santee et al., 2023) reinforce the reduction downward radiative flux. Stratospheric ozone decreases produce an increase in the shortwave flux, and this is an important contributor to the total flux. By the end of 2023 aerosols have settled out, the water vapor anomaly has largely dispersed in the lower stratosphere, and the net forcing between  $\pm 60^\circ$  has dissipated.

The Hunga eruption cooled the climate, but the amount of cooling is so small it will be difficult to extract the signal from tropospheric meteorological observations. The secondary circulation induced by stratospheric water vapor cooling altered the stratospheric temperature and ozone distribution which significantly contributed to Hunga changes in the climate forcing.

## Acknowledgements

This work was supported under NASA grants NNX14AF15G, 80NSSC21K1965 and 80NSSC20K1235. D. Zawada acknowledges the support of the Canadian Space Agency.

## Open Research

The RTM used to estimate H<sub>2</sub>O IR cooling rates is from Atmospheric and Environmental Research (RTE+RRTMG) and can be freely downloaded at [http://rtweb.aer.com/rmtm\\_frame.html](http://rtweb.aer.com/rmtm_frame.html).

OMPS data, Taha et al. (2021), is available at [https://disc.gsfc.nasa.gov/datasets/OMPS\\_NPP\\_LP\\_L2\\_AER\\_DAILY\\_2/summary](https://disc.gsfc.nasa.gov/datasets/OMPS_NPP_LP_L2_AER_DAILY_2/summary), DOI: <https://doi.org/10.5067/CX2B9NW6FI27> The algorithm is documented in Taha et al. (2021). Data are public with unrestricted access (registration required).

The OMPS USask data is available at <https://doi.org/10.5281/zenodo.7293121>

Aura MLS Level 2 data, Livesey et al. (2021) JPL D-33509 Rev. C, is available at <https://disc.gsfc.nasa.gov/datasets?page=1&keywords=AURA%20MLS>

The temperature data is available at

[https://acdisc.gesdisc.eosdis.nasa.gov/data/Aura\\_MLS\\_Level2/ML2T.004/](https://acdisc.gesdisc.eosdis.nasa.gov/data/Aura_MLS_Level2/ML2T.004/)

The V5 water vapor data is available at

[https://acdisc.gesdisc.eosdis.nasa.gov/data/Aura\\_MLS\\_Level2/ML2H2O.005/](https://acdisc.gesdisc.eosdis.nasa.gov/data/Aura_MLS_Level2/ML2H2O.005/)

## References

- Anstey, J.A., *et al.* (2022). Impacts, processes, and projections of the quasi-biennial oscillation. *Nat. Rev. Earth Environ.*, 3, 588–603, <https://doi.org/10.1038/s43017-022-00323-7>
- Aubry, T.J., Staunton-Sykes, J., Marshall, L.R. *et al.* (2021). Climate change modulates the stratospheric volcanic sulfate aerosol lifecycle and radiative forcing from tropical eruptions. *Nat. Commun.* **12**, 4708. <https://doi.org/10.1038/s41467-021-24943-7>.
- Baldwin *et al.*, (2001). The quasi-biennial oscillation, *Revs. of Geophys.*, 39, 179-229, <https://doi.org/10.1029/19999RG000073>.
- Banerjee, A., Chiodo, G., Previdi, M. *et al.* (2019). Stratospheric water vapor: an important climate feedback. *Clim Dyn* **53**, 1697–1710. <https://doi.org/10.1007/s00382-019-04721-4>
- Bourassa, A. E., Zawada, D. J., Rieger, L. A., Warnock, T. W., Toohey, M., & Degenstein, D. A. (2023). Tomographic retrievals of Hunga Tonga-Hunga Ha'apai volcanic aerosol. *Geophysical Research Letters*, 50, e2022GL101978, <https://doi.org/10.1029/2022GL101978>
- Carn, S. A., N. A. Krotkov, B. L. Fisher, and C. Li, (2022). Out of the blue: volcanic SO<sub>2</sub> emissions during the 2021-2022 Hunga Tonga – Hunga Ha'apai eruptions, *Front. Earth Sci.*, 13, <https://doi.org/10.3389/feart.2022.976962>
- Carr, J. L., A. Horváth, D. Wu, D. & M. Friberg (2022). Stereo plume height and motion retrievals for the record-setting Hunga Tonga-Hunga Ha'apai eruption of 15 January 2022. *Geophysical Research Letters*, 49, e2022GL098131. <https://doi.org/10.1029/2022GL098131>
- Cisewski, M., Zawodny, J., Gasbarre, J., Eckman, R., Topiwala, N., Rodriguez-Alvarez, O., *et al.* (2014). The stratospheric aerosol and gas experiment (SAGE III) on the International Space Station (ISS) mission. In *Sensors, systems, and next-generation satellites xviii* (Vol.9241, pp. 59–65). SPIE.
- Coy, L., P. Newman, K. Wargan, G. Partyka, S. Strahan, and S. Pawson, (2022). Stratospheric Circulation Changes Associated with the Hunga Tonga-Hunga Ha'apai Eruption, *Geophys. Res. Lett.*, 49, <https://www.essoar.org/doi/abs/10.1002/essoar.10512388.1>
- Dessler, A.E., M. R. Schoeberl, T. Wang, S. Davis, K. H. Rosenlof, (2013) Stratospheric water vapor feedback, *PNAS*, [www.pnas.org/cgi/doi/10.1073/pnas.1310344110](http://www.pnas.org/cgi/doi/10.1073/pnas.1310344110)
- Crutzen, P. J. (2006). Albedo enhancement by stratospheric sulfur injections: A

contribution to resolve a policy dilemma?, *Climatic Change*, 77, 211–  
220, <https://doi.org/10.1007/s10584-006-9101-y>.

Jenkins, S., C. Smith, M. Allen, and R. Grainger, (2023). Tonga eruption increases  
chance of  
temporary surface temperature anomaly above 1.5 °C, *Nature Climate Change*, 13,  
127–129, <https://doi.org/10.1038/s41558-022-01568-2>

Forster, P.M.D., and K. P. Shine (1999). Stratospheric water vapour changes as a  
possible contributor to observed stratospheric cooling. *Geophys. Res. Lett.*, 26,  
3309–3312.

Fujiwara, M., Martineau, P., and Wright, J. S. (2020). Surface temperature response  
to the major volcanic eruptions in multiple reanalysis data sets, *Atmos. Chem. Phys.*,  
20, 345–374, <https://doi.org/10.5194/acp-20-345-2020>.

Gelaro, R., et al. (2017). The Modern-Era Retrospective Analysis for Research and  
Applications, Version 2 [Dataset], *J. Climate*, 30, 5419–5454,  
<https://doi.org/10.1175/jcli-d-16-0758.1>.

Gorkavyi, N., Krotkov, N., Li, C., Lait, L., Colarco, P., Carn, S., et al. (2021). Tracking  
aerosols and SO<sub>2</sub> clouds from the Raikoke eruption: 3D view from satellite  
observations. *Atmospheric Measurement Techniques*, 14(12), 7545–7563.  
<https://doi.org/10.5194/amt-14-7545-2021>

Hansen, J., et al., (2002). Climate forcings in Goddard Institute for Space Studies  
SI2000 simulations, *J. Geophys. Res.*, 107(D18), 4347, doi:10.1029/2001JD001143.

Khaykin, S.M., de Laat, A.T.J., Godin-Beekmann, S. et al. (2022) Unexpected self-  
lofting and dynamical confinement of volcanic plumes: the Raikoke 2019 case.” *Sci*  
*Rep* 12, 22409. <https://doi.org/10.1038/s41598-022-27021-0>, 2022

Li, F., P. Newman (2020) Stratospheric water vapor feedback and its climate impacts  
in the coupled atmosphere–ocean Goddard Earth Observing System Chemistry-  
Climate Model. *Clim Dyn* 55, 1585–1595 <https://doi.org/10.1007/s00382-020-05348-6>

Livesey, N., Read, W.G., Wagner, P.A., Froidevaux, L., Santee, M.L., Schwartz, M.J. et al.  
(2021). Earth Observing System (EOS) Aura Microwave Limb Sounder (MLS)  
version 5.0x level 2 and 3 data quality and description document, JPL D-105336 Rev  
A. [https://mls.jpl.nasa.gov/data/v5-0\\_data\\_quality\\_document.pdf](https://mls.jpl.nasa.gov/data/v5-0_data_quality_document.pdf)

Millán, L. et al., (2022). The Hunga Tonga-Hunga Ha’apai Hydration of the  
Stratosphere, *Geophysical Research Letters*. 49,  
e2002GL099381, <https://doi.org/10.1029/2022GL099381>

- 587  
588 Mlawer, E.J., S.J. Taubman, P.D. Brown, M.J. Iacono and S.A. Clough (1997). RRTM, a  
589 validated correlated-k model for the longwave. *J. Geophys. Res.*, **102**, 16,663-16,682.  
590
- 591 Pitari, G., G. Di Genova, E. Mancini, D. Visioni, I. Gandolfi, and I. Cionni (2016).  
592 Stratospheric Aerosols from Major Volcanic Eruptions: A Composition-Climate Model  
593 Study of the Aerosol Cloud Dispersal and e-folding Time, *Atmosphere*, 7,  
594 doi:10.3390/atmos7060075.  
595
- 596 Proud, S., A. Prata, S. Schmauß (2022). The January 2022 eruption of Hunga Tonga-  
597 Hunga Ha'apai volcano reached the mesosphere, *Science*, 378. 554-557  
598 <https://www.science.org/doi/10.1126/science.abo4076>  
599
- 600 Robock, A., Volcanic Emissions and Climate, *Revs. of Geophysics*, 38, 191-219,  
601 <https://doi.org/10.1029/1998RG000054>  
602
- 603 Santee, M. L., Lambert, A., Froidevaux, L., Manney, G. L., Schwartz, M. J.,  
604 Millán, L. F., et al. (2023). Strong evidence of heterogeneous processing on  
605 stratospheric sulfate aerosol in the extra-polar Southern Hemisphere following the  
606 2022 Hunga Tonga-Hunga Ha'apai eruption. *Journal of Geophysical Research:*  
607 *Atmospheres*, 128, e2023JD039169. <https://doi.org/10.1029/2023JD039169>  
608
- 609 Schoeberl, M. R., Wang, Y., Ueyama, R., Taha, G., Jensen, E., & Yu, W. (2022).  
610 Analysis and impact of the Hunga Tonga-Hunga Ha'apai stratospheric water vapor  
611 plume. *Geophysical Research Letters*, 49, e2022GL100248.  
612 <https://doi.org/10.1029/2022GL100248>  
613
- 614 Schoeberl, M. R., Wang, Y., Ueyama, R., Taha, G., & Yu, W. (2023a). The Cross  
615 Equatorial Transport of the Hunga Tonga-Hunga Ha'apai Eruption Plume.  
616 *Geophysical Research Letters*, 49, e2022GL10443,  
617 <https://doi.org/10.1029/2022GL102443>  
618
- 619 Schoeberl, M. R., Wang, Y., Ueyama, R., Dessler, A., Taha, G., & Yu, W. (2023b). The  
620 estimated climate impact of the Hunga Tonga-Hunga Ha'apai eruption plume.  
621 *Geophysical Research Letters*, 50, e2023GL104634.  
622 <https://doi.org/10.1029/2023GL104634>  
623
- 624 Sellitto, P., A. Podglagen, R. Belhadji, M. Boichu, E. Carboni, J. Cuesta, C. Duchanp, C.  
625 Kloss, R. Siddans, N. Begue, L. Blarel, F. Jegou, S. Khaykin, H-B. Renard, and B. Legras,  
626 (2022), The unexpected radiative impact of the Hunga Tonga eruption of January 15,  
627 2022, *Commun. Earth Environ* **3**, 288 (2022). [https://doi.org/10.1038/s43247-022-](https://doi.org/10.1038/s43247-022-00618-z)  
628 [00618-z](https://doi.org/10.1038/s43247-022-00618-z)  
629
- 630 Sellitto, P., R. Siddans, R. Belhadji, E. Carboni, B. Legras, A. Podglajen, C. Duchamp,  
631 and B. Kerridge, (2024) Observing the SO<sub>2</sub> and Sulphate Aerosol Plumes from the 2022  
632 Hunga Tonga-Hunga Ha'apai Eruption with IASI, submitted to *Geophysical Res. Lett.*,



DOI:[10.22541/essoar.169091894.48592907/v1](https://doi.org/10.22541/essoar.169091894.48592907/v1)

Solomon, S., Rosenlof, R. Portmann, J. S. Daniel, S. M. Davis, T. J. Sanford, G-K. Plattner, (2010). Contributions of Stratospheric Water Vapor to Decadal Changes in the Rate of Global Warming, *Science*, 237, 1219-1221, doi:10.1126/science.1182488

Stenchikov, G. (2016). *The Role of Volcanic Activity in Climate and Global Change*, 2nd Edn., Elsevier, Boston, Massachusetts, USA, <https://doi.org/10.1016/B978-0-444-63524-2.00026-9> .

Taha, G., R. Loughman, T. Zhu, L. Thomason, J. Kar, L. Rieger, and A. Bourassa (2021). OMPS LP Version 2.0 multi-wavelength aerosol extinction coefficient retrieval algorithm, *Atmos. Meas. Tech.*, 14, 1015–1036, <https://doi.org/10.5194/amt-14-1015-2021>.

Taha, G., R. Loughman, P. Colarco, T. Zhu, L. Thomason, G. Jaross (2022). Tracking the 2022 Hunga Tonga-Hunga Ha'apai aerosol cloud in the upper and middle stratosphere using space-based observations, *Geophys. Res. Lett.*, <https://doi.org/10.1029/2022GL100091>.

Tao, M., Konopka, P., Ploeger, F., Grooß, J. U., Müller, R., Volk, C. M., et al. (2015). Impact of the 2009 major sudden stratospheric warming on the composition of the stratosphere. *Atmospheric Chemistry and Physics*, 15(15), 8695–8715. <https://doi.org/10.5194/acp-15-8695-2015>

Veenus, V., Das, S. S., & David, L. M. (2023). Ozone changes due to sudden stratospheric warming-induced variations in the intensity of Brewer-Dobson circulation: A composite analysis using observations and chemical-transport model. *Geophysical Research Letters*, 50, e2023GL103353. <https://doi.org/10.1029/2023GL103353>

Vömel, H., S. Evan, and M. Tully (2022). Water vapor injection into the stratosphere by Hunga Tonga-Hunga Ha'apai, *Science*, 377,1444-1447.

Wang, X., Randel, W., Zhu, Y., Tilmes, S., Starr, J., Yu, W., et al. (2023). Stratospheric climate anomalies and ozone loss caused by the Hunga Tonga-Hunga Ha'apai volcanic eruption. *Journal of Geophysical Research: Atmospheres*, 128, e2023JD039480. <https://doi.org/10.1029/2023JD039480>

Wilmouth, D., F. Østerstrøm, J. Smith, J. G. Anderson, & R. Salawitch, (2023). Impact of the Hunga Tonga volcanic eruption on stratospheric composition, *PNAS*, 120, e2301994120, <https://doi.org/10.1073/pnas.2301994120>.

Yu, Q., & Huang, Y. (2023). Distributions and trends of the aerosol direct radiative

effect in the 21st century: Aerosol and environmental contributions. Journal of  
Geophysical Research: Atmospheres, 128, e2022JD037716.  
<https://doi.org/10.1029/2022JD037716>

Yu, W., Garcia, R., Yue, J., Smith, A., Wang, X., Randel, W., et al. (2023). Mesospheric  
temperature and circulation response to the Hunga Tonga-Hunga Ha'apai volcanic  
eruption. Journal of Geophysical Research: Atmospheres, 128, e2023JD039636.  
<https://doi.org/10.1029/2023JD039636>

Zhu et al., (2022). Perturbations in stratospheric aerosol evolution due to the water-  
rich plume of the 2022 Hunga-Tonga eruption, Communications Earth &  
Environment, 3, 248, <https://doi.org/10.1038/s43247-022-00580-w>

692

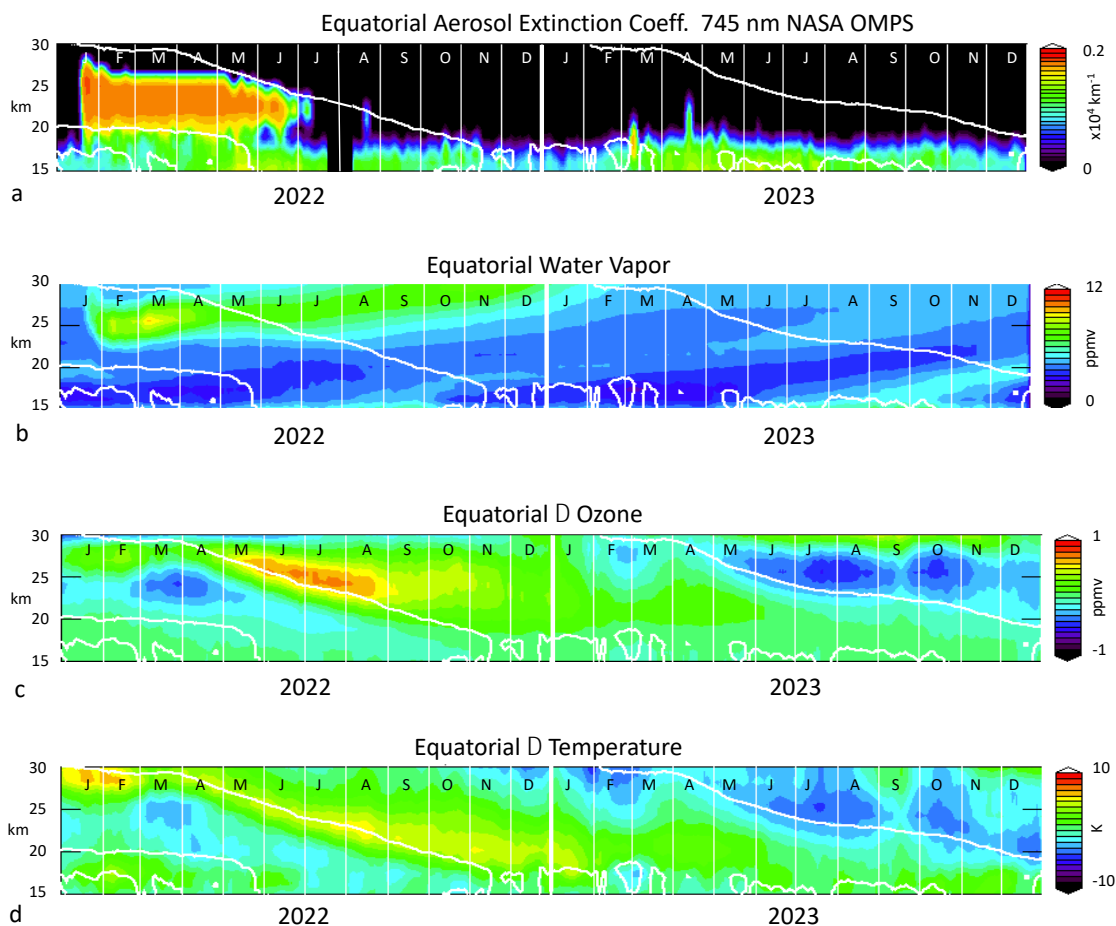


Fig. 1

Figure 1 Equatorial cross section of aerosols and trace gases. Part a 745 nm extinction coefficient ( $\text{km}^{-1}$ )  $\pm 1^\circ$  of the equator. Part b, water vapor, Part c  $\Delta$  ozone (difference from 10-year climatology). Part d,  $\Delta$  temperature all  $\pm 2.5^\circ$  of the equator. Month letters starting 2022 are shown in the figure. Months are show as first letters and monthly regions are divided by white lines. The thick white line is the equatorial zero wind line from MERRA2 assimilation. Color bars indicate the scale.

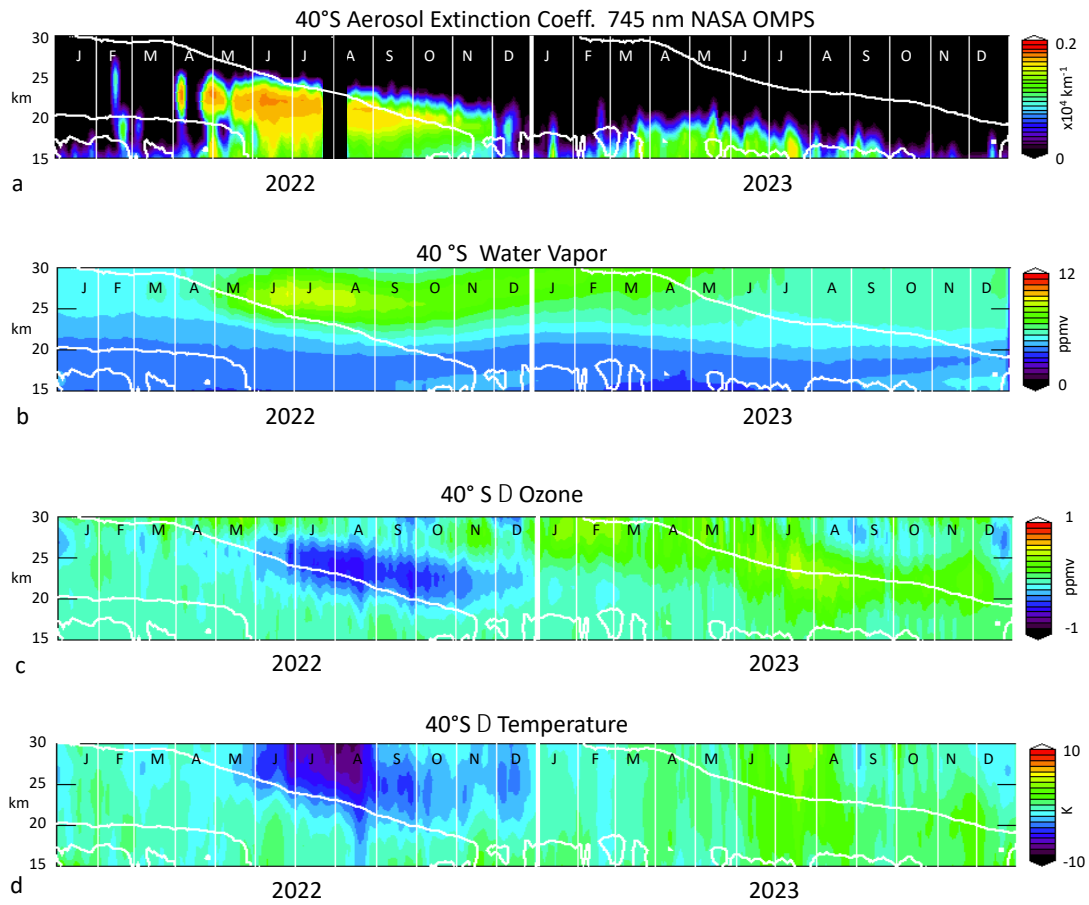


Fig. 2

Figure 2. Same as Fig. 1 at 40° S

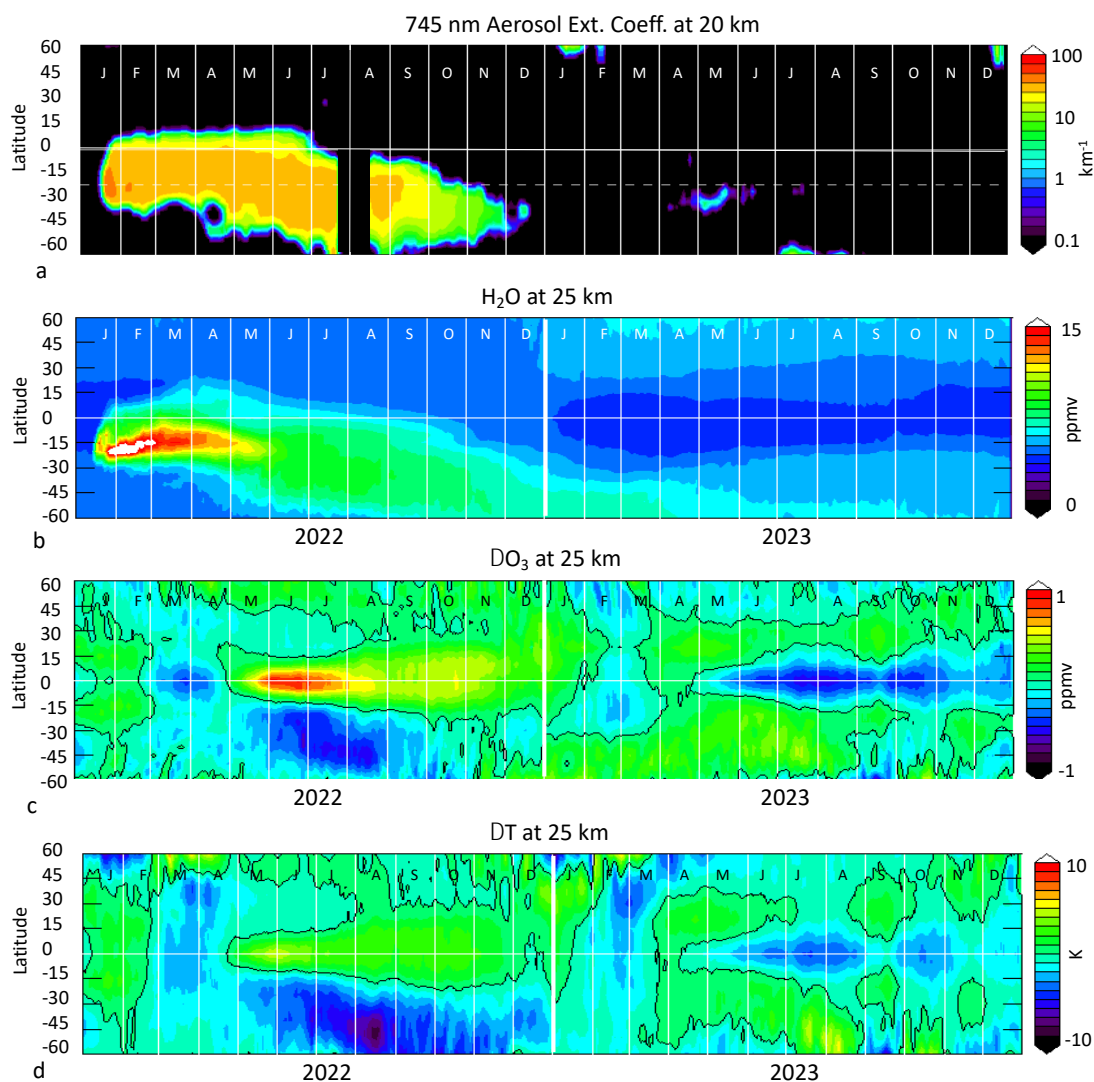


Fig. 3

Figure 3 Constituent zonal mean fields. Part a, aerosol extinction coefficient at 20 km. Parts b-d at 25 km. Part b, water vapor, Part c  $\Delta$  ozone, Part c  $\Delta$  temperature. Thin white horizontal line indicates the equator. Thick black line contour is zero in parts d and d.

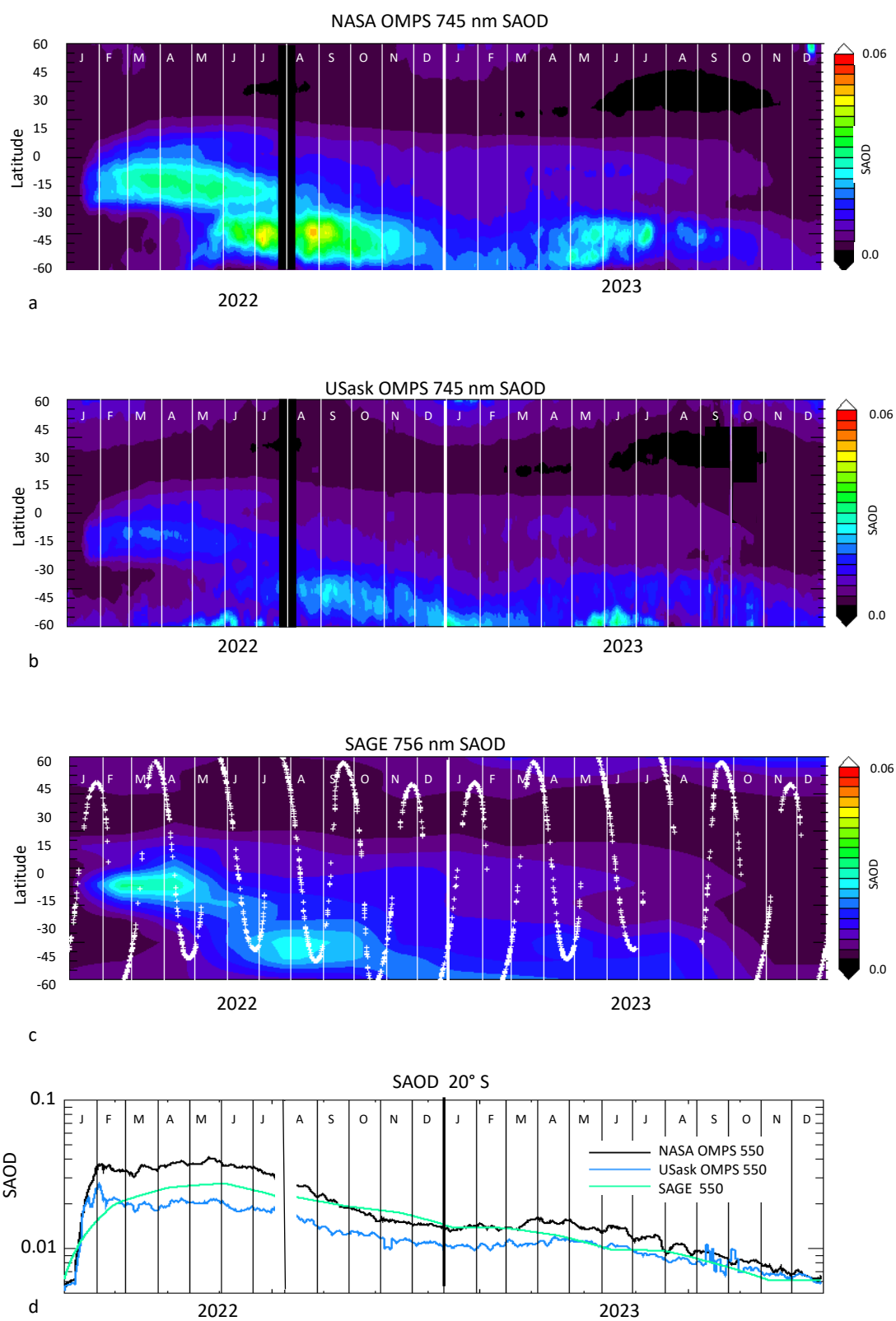


Fig. 4

709 Figure 4 Zonal mean SAOD time series. Part a, NASA OMPS, Part b, USask OMPS, both at 745 nm. Part c, SAGE  
 710 III/ISS SAOD at 756nm interpolated onto the OMPS grid. Part d shows the 20°S SAOD converted to 550nm using the  
 711 SAGE Ångström exponent from Parts a, b, and c.

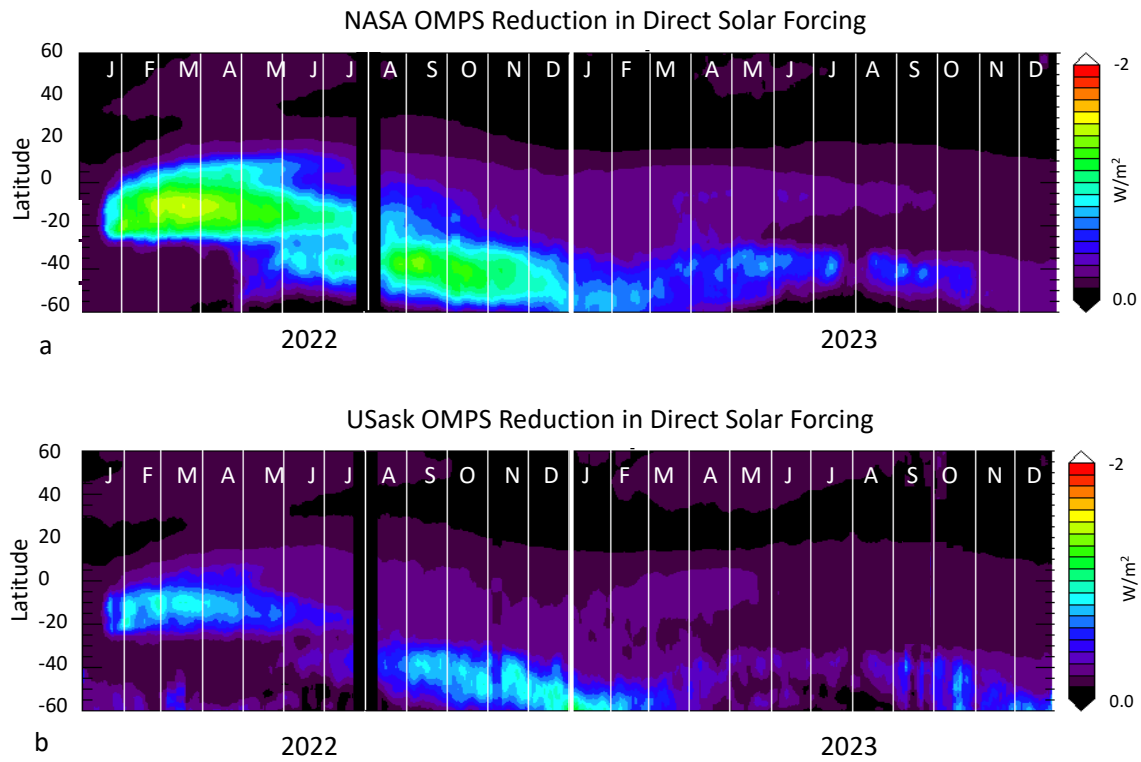


Fig. 5

712  
 713  
 714 Figure 5 Part a, direct forcing from NASA OMPS SAOD. Part b, direct forcing using USask SAOD

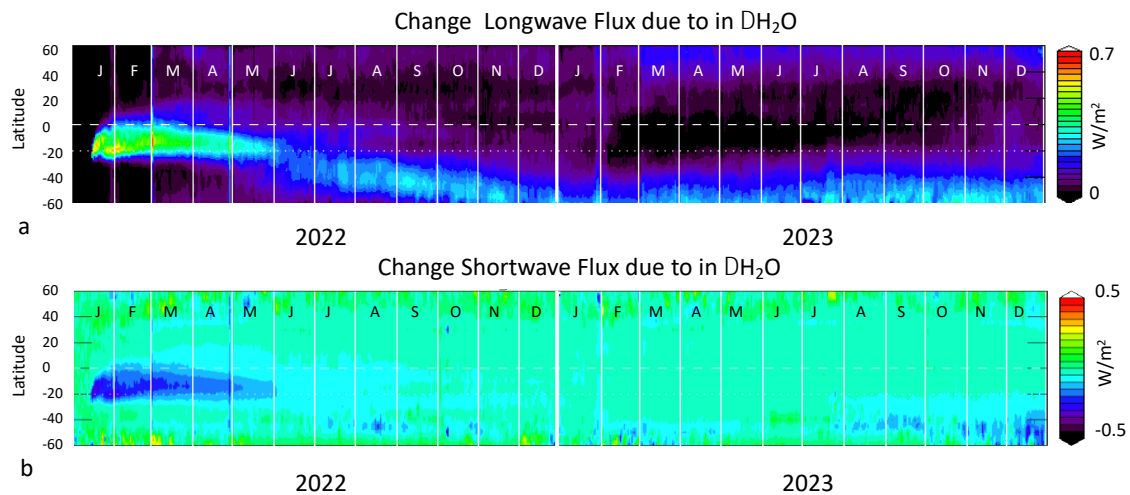


Fig. 6

715

716 Figure 6 Part a, change in long-wave IR flux from climatology due to water vapor. Part b, change in short-wave flux.  
 717 Months indicated as in Fig. 1.

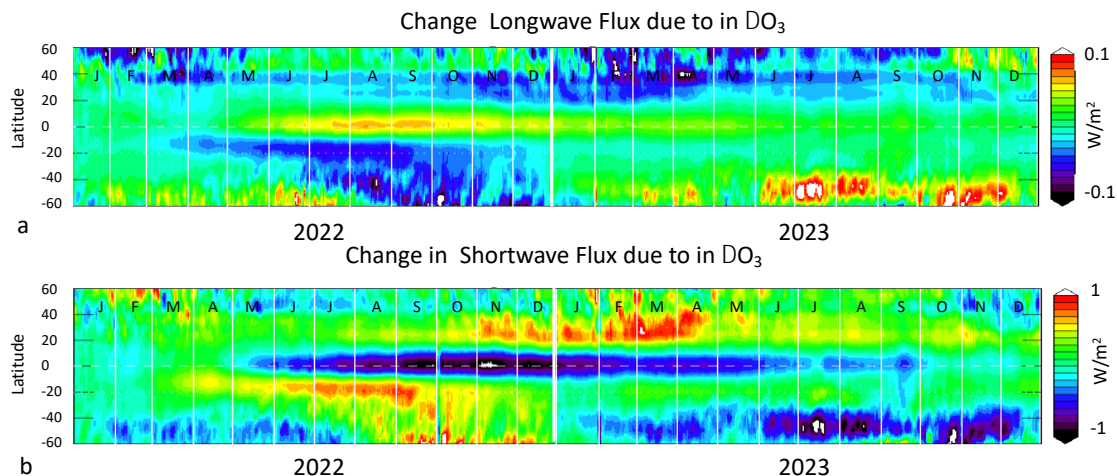


Fig. 7

718  
 719  
 720 Figure 7 fluxes due to change in ozone; Part a, longwave, Part b, shortwave.

721

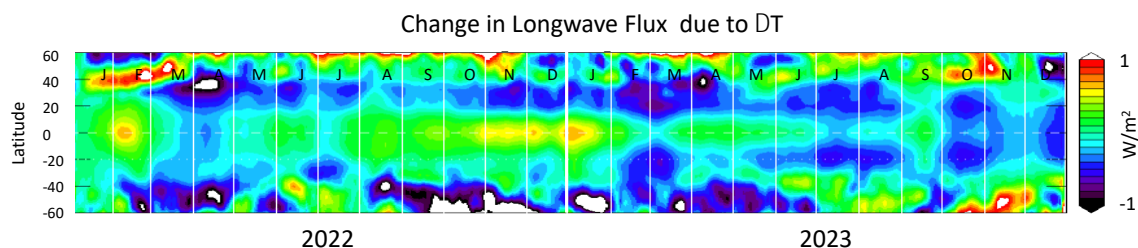


Fig. 8

722  
 723 Figure 8 As in Fig. 7a but for change in temperature.



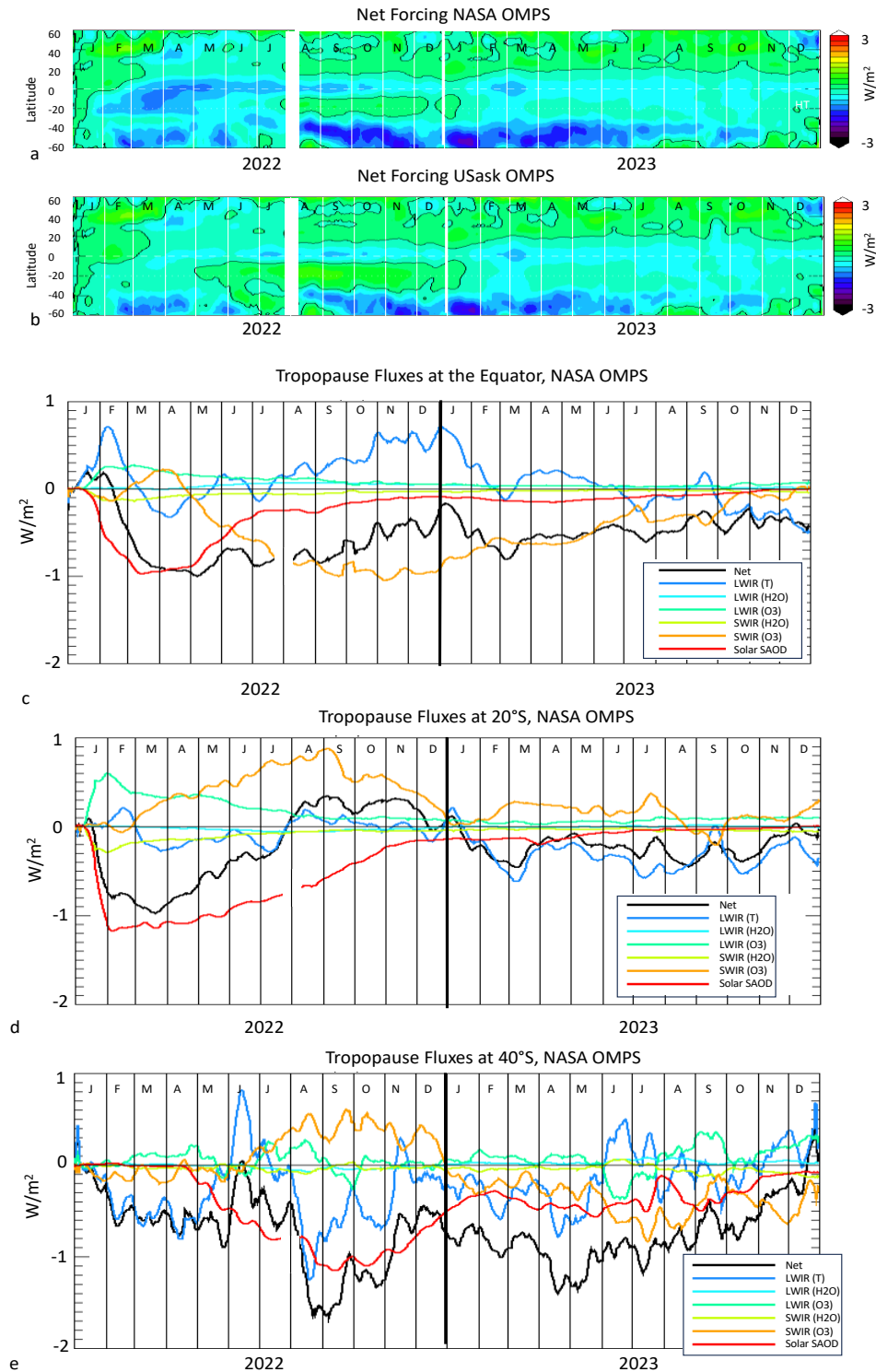


Figure 9 Part a. Net forcing including trace gas fluxes and aerosol direct forcing using NASA OMPS SAOD. Part b is similar to (a) but for USask SAOD. Parts c, d, e show the various flux components at the equator (Part b), 20°S (Part c) and 40°S (Part d) using NASA OMPS SAOD.

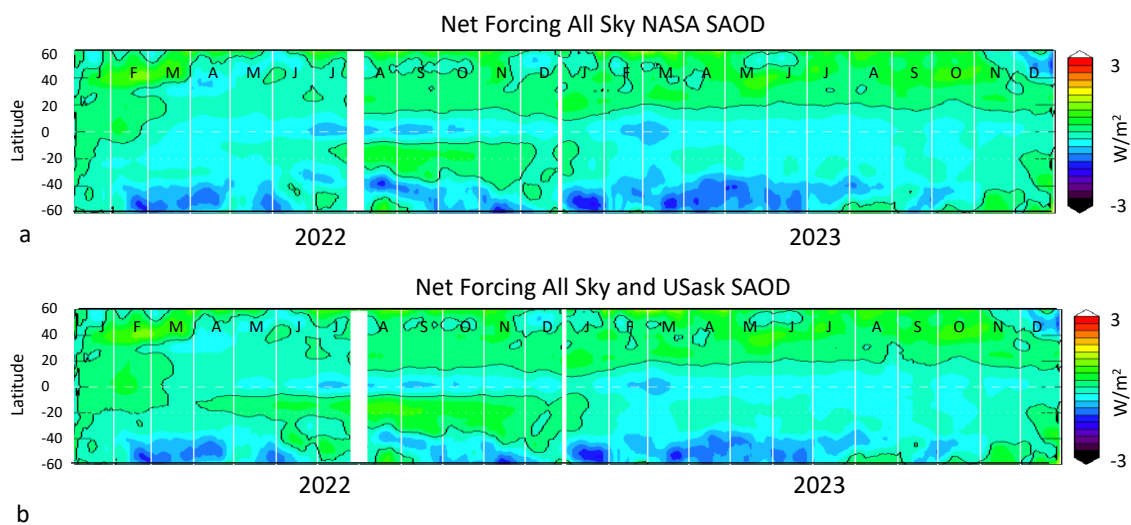


Fig. 10

Figure 10. Net forcing using all sky albedo. Part a with NASA OMPS SAOD. Part b, USask OMPS SAOD.

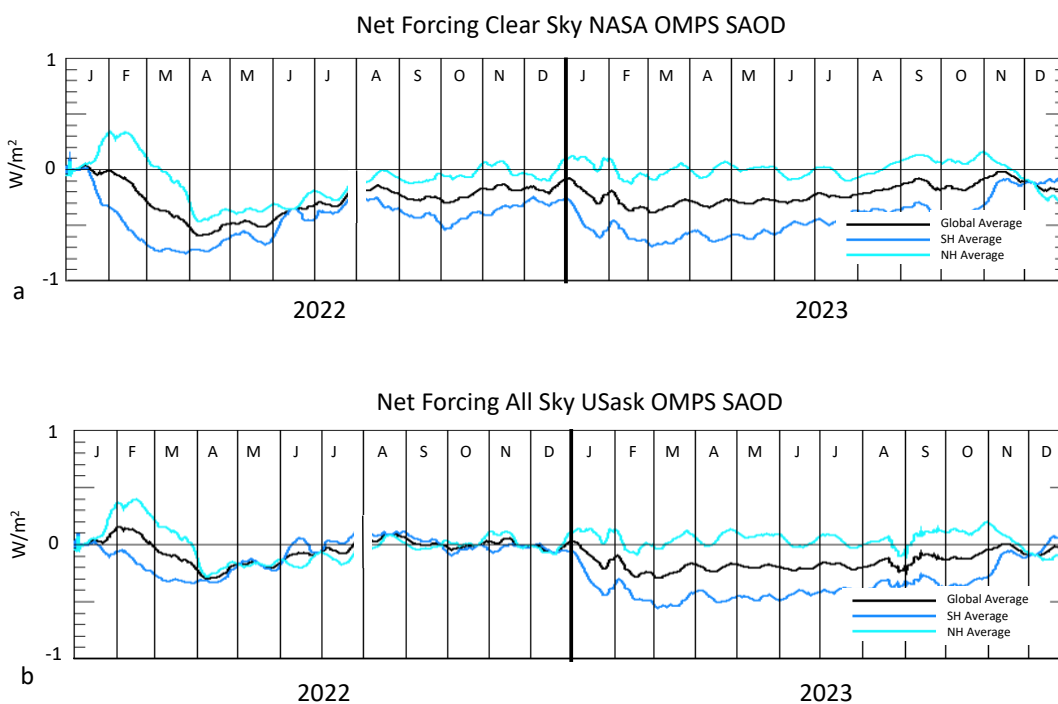


Fig. 11

Figure 10 Variations of global (black), SH (blue) and NH (cyan) downward fluxes. Part a, clear sky, NASA OMPS SAOD (see Fig. 9a). Part b, all sky USask SAOD (Fig. 10b).